Optimized Design of Full-Bridge Modular Multilevel Converter With Low Energy Storage Requirements for HVdc Transmission System

Cong Zhao, *Student Member, IEEE*, Yaohua Li, Zixin Li, *Senior Member, IEEE*, Ping Wang, Xun Ma, and Yongjie Luo

***Abstract*—Modular multilevel converter (MMC) is a well-proved circuit topology in voltage-source converter-based high voltage direct current (VSC-HVdc) transmission systems. As is known, the conventional half-bridge submodule (HBSM)-based MMC-HVdc is not suitable for overhead line transmission applications. In addition, high energy storage requirements, i.e., large capacitance is inevitable. The conventional design of the full-bridge submodule (FBSM)-based MMC usually does not utilize the negative voltage state of FBSM in normal operation. Considering the same dc voltage as with the HBSM case and utilizing the negative voltage state of the FBSM, this paper presents the design method of the power transmission capability of a single FBSM. Meanwhile, an optimized energy storage capacitance design method of the FBSM is proposed. With this method, the capacitance of FBSM can be reduced significantly. The correctness and effectiveness of the proposed method is verified by the simulation of a ±160 kV VSC-HVdc MMC and the comparison results of the dc short fault blocking and ride through capability are also provided.**

***Index Terms*—Full-bridge submodule (FBSM), low energy storage requirements, modular multilevel converter (MMC), optimization design method.**

I. Introduction

In HIGH voltage direct current (HVdc) transmission applications, voltage-source converter (VSC) is superior to conventional line commutated converter in terms of constant dc voltage polarity, independent control of active and reactive power, no problem of commutation failure and so on [1], [2]. Modular multilevel converter (MMC) which was first presented by Marquardt in 2003 [3] is a promising converter topology. Compared to the conventional two-level or three-level converters, MMC is an attractive circuit topology in high voltage and high power applications, due to its low harmonics, scalability, high reliability, and high efficiency [4]–[7]. Hence, MMC is widely adopted in many VSC-HVdc transmission projects [8].

Manuscript received June 8, 2016; revised August 24, 2016 and October 22, 2016; accepted January 17, 2017. Date of publication January 27, 2017; date of current version October 6, 2017. Recommended for publication by Associate Editor M. Tavakoli Bina. *(Corresponding author: Zixin Li.)*

The authors are with the Key Laboratory of Power Electronics and Electric Drive, Institute of Electrical Engineering, Chinese Academy of Sciences, Beijing 100190, China (e-mail: zhaocong@mail.iee.ac.cn; yhli@mail.iee.ac.cn; lzx@mail.iee.ac.cn; wangping@mail.iee.ac.cn; maxun@mail.iee.ac.cn; luoyongjie@mail.iee.ac.cn).

Color versions of one or more of the figures in this paper are available online at http://ieeexplore.ieee.org.

Digital Object Identifier 10.1109/TPEL.2017.2660532

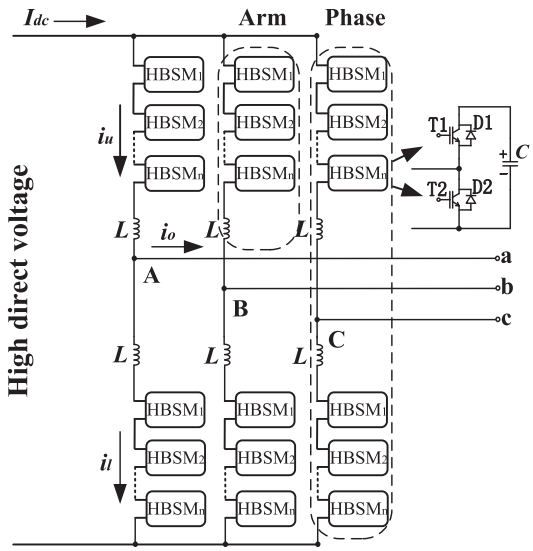

Fig. 1. Simplified schematic diagram of H-MMC.

The simplified schematic of the half-bridge submodule (HBSM)-based MMC (H-MMC) in HVdc systems is presented in Fig. 1. When dc short-circuit fault occurs, the voltage of dc positive and negative voltage becomes almost zero. Low impedance leads high ac currents to flow through the freewheeling diodes from the ac side to the dc side even when all power devices are turned off [9]. The arm currents increase rapidly causing serious damage to the MMC. Hence, how to deal with the dc short-circuit faults is one of the main concerns in HVdc transmission systems, especially in the overhead line applications. Generally, there are two methods about handling the dc short-circuit faults in order to ensure safety operation of the MMC. The first one is the ac or dc circuit breaks (CBs) employed so as to disconnect the MMC from the fault point or ac-side grid. The response of the conventional ac CBs is not fast enough for fault isolation [10]. The power devices bear excessive current stress during the responding time. Several solid-state dc CBs have been proposed in [11]–[13] which can cut off fault current in a very short period of time. However, the dc CBs are extremely expensive and the on-state operational losses are significantly high owing to the power devices in the current path [14]. Hence, the dc CB is still very far from the wide range of applications.

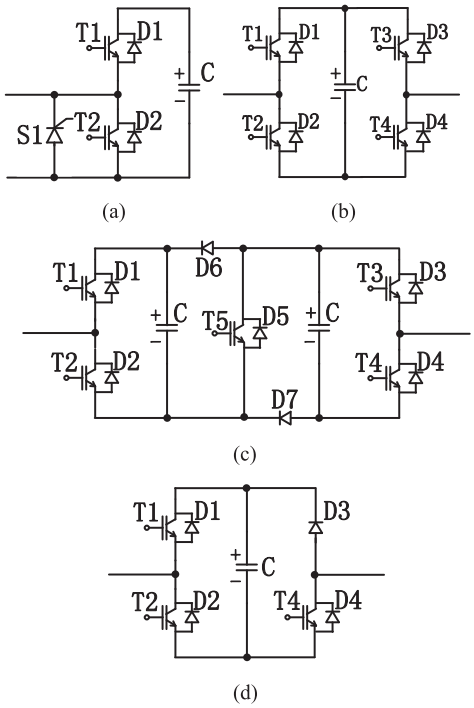

Fig. 2. Different types of SM topology.

The second method is embedding the dc fault handing capability converter topology. Employing antiparallel thyristors at the SM terminal shown in Fig. 2(a) has been proposed in [15] for protecting the freewheel diodes. But it does not achieve fault isolation. Replacing every HBSM with full-bridge submodule (FBSM) presented in Fig. 2(b) [16], [17] can provide fault ride through capability which is operated as a STATCOM when dc short circuit happens. It is also able to block fault current if all power semiconductors are turned off when dc short-circuit faults occur. However, FBSM-based MMC (F-MMC) utilizes twice number of insulated-gate bipolar transistors (IGBTs) than H-MMC which leads to higher conduction losses. In [18], a new submodule provided in Fig. 2(c) called clamp double submodule (CDSM) was proposed employing which can block fault current. But this topology cannot support ac grid during dc short-circuit faults. In Fig. 2(d), the principle of the unipolar-voltage FBSM proposed in [19] is the same as the CDSM. In order to trade off power losses and fault ride through capabilities, a new hybrid MMC topology mixed with HBSMs and FBSMs was proposed in [19]. This topology can achieve fault ride through capability [20]–[22] with less cost of power semiconductors and lower losses. Its design and operation principles with utilizing the negative voltage state of FBSMs were presented in [23].

In HVdc scenarios, each arm of MMC often contains hundreds of SMs. Huge number of power devices and capacitances are necessary for power transmission. Moreover, large capacitance of SM capacitor which is bulky and costly is needed considering voltage ripples especially when the rated power is high. In [24], a method to estimate the capacitance was presented combining voltage ripple with energy variation. The relationship between circulating currents and SM voltage ripples was analyzed in detail in [25]. The direct relation between the energy stored in SM capacitors and the power transferred by MMC was derived and the minimal energy storage requirements of SM capacitance were analyzed in different power factor angles situations in [26]. In [27], the dimensioning of SM capacitors in MMC was derived based on analytical equations and the minimal energy storage requirements of SM capacitance were also presented. In addition, authors in [28] and [29] provided a strategy by circulating current injection in order to minimize the SM capacitance. Picas *et al.* [30] proposed a closed-loop discontinuous modulation technique for SM capacitor voltage ripples reduction based on zero-sequence injected to the original modulation signals. In [31], another circulating current injection method was proposed in terms of increasing modulation index and it achieved about 25% relative ripple reduction.

So far, few studies have investigated the power transmission capability of the F-MMC without and with using negative voltage state of FBSMs under the same RMS of arm currents and dc voltage conditions. Besides, circulating current and zero-sequence injection are the main two methods to minimize SM capacitance according to previous depiction. Even though some studies have considered the negative voltage state of FBSMs, fewer literatures have focused on how it will affect capacitor voltage ripples. In this paper, the power transmission capability of a single FBSM of the F-MMC with and without using the negative voltage state is analyzed comparatively under the same dc voltage and RMS of arm currents conditions. The optimal method is provided according to which the power transmission capability will reach the maximum. Furthermore, the FBSM voltage fundamental frequency and second-order harmonic fluctuations are also studied comparatively. It is found that the fundamental frequency fluctuations are almost suppressed with negative voltage state generated by FBSM when the power factor of the converter is close to one. Thus, the FBSM capacitance is reduced significantly and the optimization method is also presented. In terms of these two optimization methods, the main contribution of this paper is to reduce the FBSM capacitance which aims to provide a space-saving and cost-effective converter for HVdc transmission systems.

The rest of this paper is as follows. The basic operation of the F-MMC utilizing negative voltage state of FBSM is introduced in Section II. In Section III, the comparative power transmission capability of a single FBSM of the F-MMC with and without utilizing the negative voltage state is derived under the same dc voltage and RMS of arm currents conditions. This is followed by an optimized method for reducing FBSM capacitance in Section IV. The FBSM capacitor voltage fundamental frequency and second-order harmonic fluctuations resulted by circulating currents and the arm inductor design are presented in Section V. In Section VI, computer simulation results are provided with the comparative research of a $\pm$160 kV F-MMC rectifier. Finally, the conclusions are drawn in Section VII.

II. Operation Principle of F-MMC

The simplified schematic of the F-MMC is shown in Fig. 3. The F-MMC consists of three phases, each formed by the upper arm and the lower arm. Each arm is composed of a number of

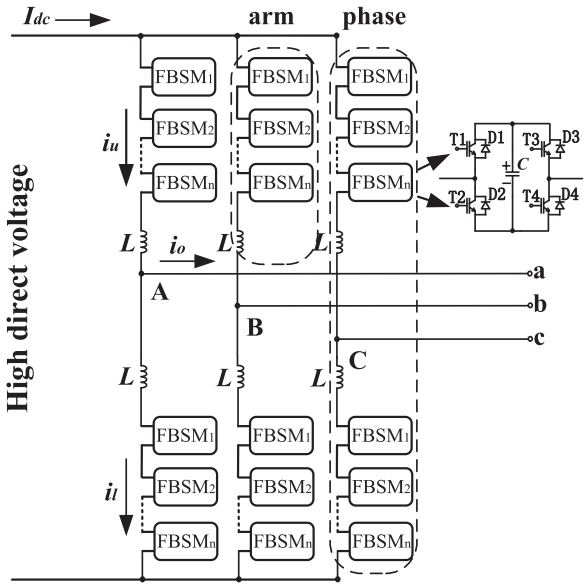

Fig. 3. Simplified schematic diagram of F-MMC.

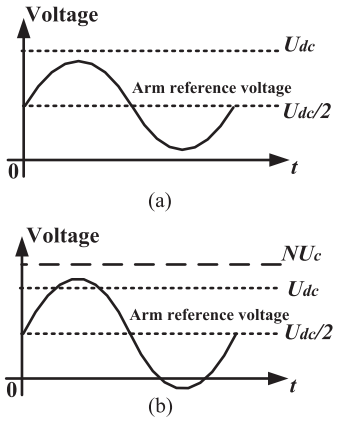

Fig. 4. Arm reference voltage and dc voltage of F-MMC.

series-connected FBSMs and an inductor. As known, the arm reference voltage of H-MMC is composed of dc and fundamental frequency components. The components of F-MMC's arm reference voltage are similar to H-MMC while the amplitude of the ac-side voltage of F-MMC is greater than H-MMC with utilizing negative voltage state of FBSMs if they have the same dc voltage. Taking the upper arm of the F-MMC shown in Fig. 3 as an example, the F-MMC with the relation curve between the arm reference voltage and the dc voltage presented in Fig. 4(a) is named as F1-MMC. Correspondingly, defining F2-MMC is the one with the curve depicted in Fig. 4(b). It needs to be added that F1-MMC has no significant difference with H-MMC in terms of SM voltage balancing for its arm reference voltages which are always greater than zero. Positive arm current charges FBSM capacitor if inserted while it is discharged with negative arm current according to the current direction definition in Fig. 3. Therefore, FBSMs with the lowest voltages are selected to be inserted when arm current is positive and the highest ones are chosen to be triggered with negative arm current. However, there are some differences for FBSM voltage balancing of F2-MMC. It is the same as F1-MMC when the arm reference voltage of F2-MMC is positive. For negative parts, it is opposite. That is to say the FBSM capacitor is discharged with positive arm current and it is charging by negative arm current if inserted. Thus, FBSMs with the highest voltages should be inserted in case of positive arm current while the lowest ones are selected when arm current is negative.

In HVdc systems, dc voltage is an important indicator which relates to line losses. Assuming that the F1-MMC and the F2-MMC have the same dc voltage which is marked as $U_{\rm dc}$. The modulation index and their FBSM reference voltages are both *m* and U_c. According to Fig. 4(b), the following expression can be achieved:

$$\frac{U_{o2}+\frac{U_{\rm dc}}{2}}{N_2U_c}=m \tag{1}$$

$$\frac{U_{\rm dc}}{2}=U_{o2}-N_0U_c \tag{2}$$

where U_{o2} is the amplitude of ac-side phase voltage for F2-MMC and N_2 is the number of FBSMs per arm. Additionally, N_0 is the ratio of the negative maximum value of the arm reference voltage shown in Fig. 4(b) to U_c. It is defined that the variable α is equal to N_0/N_2. Solving (1) and (2), the dc-side voltage and the amplitude of ac-side phase voltage are

$$U_{\rm dc}=\ (m-\alpha)N_2U_c \tag{3}$$

$$U_{o2}=\ \frac{(m+\alpha)}{2}N_2U_c. \tag{4}$$

The ac-side three-phase power and the dc-side power satisfy the following equation according to power conservation neglecting the converter losses. That is given by

$$U_{\rm dc}I_{\rm dc\ 2}=\frac{3}{2}U_oI_{o2}\cos\varphi \tag{5}$$

where φ is the power factor angel for F2-MMC. $I_{\rm dc2}$ and I_{o2} are the amplitude of the dc-side current and the ac-side current of F2-MMC, respectively. Substituting (3) and (4) into (5), the dc-side current and the amplitude of ac-side current should meet the following criteria:

$$I_{\rm dc2}=\frac{3}{4}kI_{o2}\cos\varphi \tag{6}$$

where *k* is defined as follows:

$$k=\frac{m+\alpha}{m-\alpha}. \tag{7}$$

Formulas (1)–(7) demonstrate that the voltage and current of the dc and ac side of F2-MMC also depend on the variable α if both F1-MMC and F2-MMC have the same modulation index.

III. Optimization of Parameter for Transmission Capability

According to Fig. 4(a) and (b), the number of FBSMs per arm and the ac-side voltage of the F2-MMC should be greater than the F1-MMC if they have the same dc voltage and FBSM average voltage. It is necessary to analyze the maximum capacity

of the F2-MMC compared with the F1-MMC under the same modulation index and RMS of arm current conditions. Both F1-MMC and F2-MMC have the same dc voltage according to previous assumption. The following equation must be satisfied:

$$(m-\alpha)N_2U_c = N_1U_c \tag{8}$$

where N_1 is the number of FBSMs per arm for F1-MMC. The proportion of the number of FBSMs per arm of F2-MMC and F1-MMC can be achieved from (8). That is given by

$$\eta = \frac{N_2}{N_1} = \frac{1}{m-\alpha}. \tag{9}$$

Formula (9) demonstrates that the number of FBSMs per arm of the F2-MMC increases with the variable α increasing under the same dc voltage constraints. Only dc and fundamental frequency components are considered in the arm currents since the amplitude of circulating current is often small. If the RMS of arm currents of the F1-MMC and F2-MMC are equal, the following equation can be derived:

$$\left(\frac{I_{o2}}{2\sqrt{2}}\right)^2 + \left(\frac{kI_{o2}}{4}\cos\varphi\right)^2 = \left(\frac{I_{o1}}{2\sqrt{2}}\right)^2 + \left(\frac{mI_{o1}}{4}\cos\varphi\right)^2 \tag{10}$$

where I_{o1} is the amplitude of the ac-side current for F1-MMC. The proportion of I_{o2} and I_{o1} is acquired from (10) which yields

$$\frac{I_{o2}}{I_{o1}} = \sqrt{\frac{2+m^2\cos^2\varphi}{2+k^2\cos^2\varphi}}. \tag{11}$$

Hence, the proportion of the power transferred by the F2-MMC and the F1-MMC is expressed as follows:

$$\gamma = \frac{U_{o2}I_{o2}}{U_{o1}I_{o1}}. \tag{12}$$

In (12), U_{o1} is equal to $mN_1U_c/2$. Substituting (4), (9), and (11) into (12), the expression of the power ratio of F2-MMC and F1-MMC can be obtained. That is given by

$$\gamma = \frac{m+\alpha}{m(m-\alpha)}\sqrt{\frac{2+m^2\cos^2\varphi}{2+k^2\cos^2\varphi}}. \tag{13}$$

It is defined as a function which consists of the power ratio shown in (13) divided by (9). The function investigates the F2-MMC power transmission capability of a single FBSM compared with the F1-MMC. The expression of the function is written in the following form:

$$\Gamma = \frac{m+\alpha}{m}\sqrt{\frac{2+m^2\cos^2\varphi}{2+k^2\cos^2\varphi}}. \tag{14}$$

It is concluded that the F2-MMC power transmission capability of a single FBSM is higher than the F1-MMC if the value of the function is greater than one. It is lower when the value is smaller than one.

In HVdc systems, the power factor is very close to one, especially in high-power applications. Taking the actual project of ±350 kV/1044 MVA MMC for a back-to-back HVdc system interconnecting two 500 kV ac power grids in south China [32] as an example, the rated active and reactive power of the converter is 1000 MW and 300 MVar, respectively. The power factor is as high as 0.96 under rated condition. Therefore, it is reasonable that cos φ in (14) is considered to be one approximately. Generally, the modulation index often ranges from 0.8 to 1. The maximum of the variable α is consider as 0.33 for the dc-side voltage of F2-MMC should not be too low according to (3) in Section II. Hence, the function is considered as a function of *m* and α and its 3-D surface is depicted by MATLAB which is shown in Fig. 5.

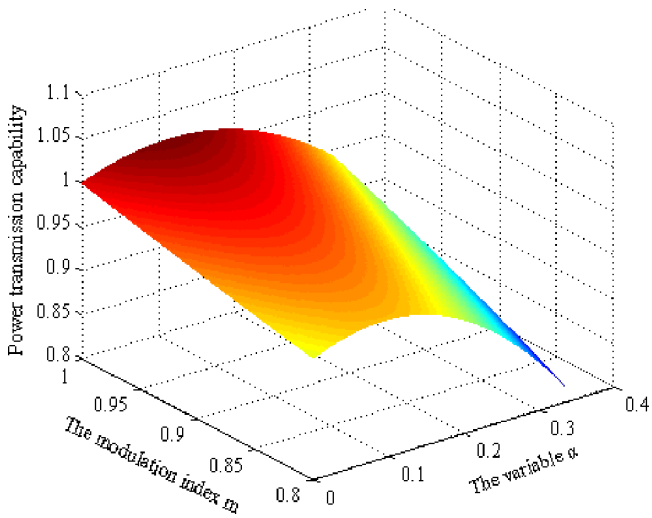

Fig. 5. F2-MMC power transmission capability of a single FBSM compared with the F1-MMC.

Fig. 5 demonstrates that the F2-MMC power transmission capability of a single FBSM is very close to the F1-MMC when the modulation index is greater than 0.9. The power transmission capability is higher when the modulation index is higher than 0.95 according to Fig. 5. The value of the function in (14) is 0.99 when the modulation index *m* and the variable α are sat as 0.9 and 0.15, respectively. It is also concluded that the value of the function increases first with the variable α increasing. Then, the proportion decreases if α continue to increase. However, the function does not increase obviously with the modulation index *m* increasing while it varies significantly with the variable α. Furthermore, the function always reaches the maximum when α ranges from 0.1 to 0.2 under different modulation index conditions. Hence, the proportion can be seen as a function about single variable α considering that the power factor is one. Formula (14) is rewritten in the following form which is given by

$$\Gamma(\alpha) = \frac{m+\alpha}{m}\sqrt{\frac{2+m^2}{2+k^2}}. \tag{15}$$

Calculating the derivation of the function in (15), that is

$$\frac{d\Gamma(\alpha)}{d\alpha} = 0. \tag{16}$$

Substituting (7) into (16), the value of the variable α which is expressed as follows can be achieved when the function reaches

the maximum:

$$\alpha = \frac{\sqrt[3]{2}-1}{\sqrt[3]{2}+1}m. \tag{17}$$

Formula (17) demonstrates that the F2-MMC power transmission capability of a single FBSM reaches the maximum when the amplitude of the negative voltage is $0.115m$ of the sum of the voltage generated by all FBSMs in one arm. Furthermore, the power transmission capability of a single FBSM of F1-MMC and F2-MMC has almost no difference if the modulation index is equal to or greater than 0.9. This conclusion is drawn under the unity power factor conditions. In case of nonunity power factor situations, the function is closer to one according to (14). Hence, the F2-MMC is particularly suitable to be operated with high modulation index in order to achieve high power transmission capability in case that the dc voltage and RMS of arm currents are the same as F1-MMC.

IV. Optimization of FBSM Capacitance

In this section, the FBSM voltage fundamental frequency and second-order harmonic fluctuations of the F2-MMC are analyzed in comparison with the F1-MMC. The arm currents of the F2-MMC are similar to the F1-MMC which are mainly composed of dc and fundamental frequency components. Taking the upper arm of phase A as an example, the relationship between the dc-side current and ac-side current of the F2-MMC is acquired according to (6) and the direction definition of the current in Fig. 3. Supposing that the upper arm currents of the F2-MMC and F1-MMC are i_{au2} and i_{au1} which yields

$$i_{au2} = \frac{I_{o2}}{4}\frac{m+\alpha}{m-\alpha}\cos\varphi + \frac{I_{o2}}{2}\cos(\omega t-\varphi) \tag{18}$$

$$i_{au1} = \frac{I_{o1}}{4}m\cos\varphi + \frac{I_{o1}}{2}\cos(\omega t-\varphi) \tag{19}$$

where I_{o1} is the amplitude of ac-side current of F1-MMC. Similarly, the equivalent switching function of the upper arm of phase A of the F2-MMC and the F1-MMC is

$$S_{au2} = \frac{\frac{U_{\rm dc}}{2} - U_{o2}\cos\omega t}{N_2 U_c} = \frac{m-\alpha}{2}\left(1-\frac{m+\alpha}{m-\alpha}\cos\omega t\right) \tag{20}$$

$$S_{au1} = \frac{\frac{U_{\rm dc}}{2} - U_{o1}\cos\omega t}{N_1 U_c} = \frac{1}{2}(1-m\cos\omega t). \tag{21}$$

Assume that all FBSM voltages are always balanced well. It is defined that the FBSM voltage of the upper arm of the F2-MMC and F1-MMC is $u_{\rm cau2}$ and $u_{\rm cau1}$. It is easily achieved that by integrating the arm current and the equivalent switching function yields

$$u_{cau2} = U_c + \frac{1}{C}\int S_{au2}i_{au2}dt \tag{22}$$

$$u_{cau1} = U_c + \frac{1}{C}\int S_{au1}i_{au1}dt. \tag{23}$$

Substituting (18) and (20) into (22), the expression of the FBSM voltage of the F2-MMC is obtained as follows if the FBSM capacitance is C:

$$u_{cau2} = U_c + \frac{m-\alpha}{2C}\left[-\frac{(m+\alpha)^2 I_{o2}\cos\varphi}{4\omega(m-\alpha)^2}\sin\omega t + \frac{I_{o2}}{2\omega}\sin(\omega t-\varphi) - \frac{(m+\alpha)I_{o2}}{8\omega(m-\alpha)}\sin(2\omega t-\varphi)\right]. \tag{24}$$

Correspondingly, the FBSM voltage of the F1-MMC is achieved by substituting (19) and (21) into (23):

$$u_{cau1} = U_c + \frac{1}{2C}\left[-\frac{m^2 I_{o1}\cos\varphi}{4\omega}\sin\omega t + \frac{I_{o1}}{2\omega}\sin(\omega t-\varphi) - \frac{mI_{o1}}{8\omega}\sin(2\omega t-\varphi)\right]. \tag{25}$$

Assume that ε_{f1} and ε_{f2} are the fundamental frequency ripple factors of the F1-MMC and F2-MMC, respectively. Calculating the fundamental frequency fluctuations of the FBSM voltage in (24) and (25), they are given by

$$\varepsilon_{f2} = \frac{I_{o2}\sqrt{(m^2+\alpha^2-6m\alpha)^2\cos^2\varphi + 4(m-\alpha)^2\sin^2\varphi}}{8(m-\alpha)\omega C U_c} \tag{26}$$

$$\varepsilon_{f1} = \frac{I_{o1}\sqrt{(2-m^2)^2\cos^2\varphi + 4\sin^2\varphi}}{8\omega C U_c}. \tag{27}$$

According to (11), the proportion of the FBSM voltage fundamental frequency fluctuations of the F2-MMC and F1-MMC is obtained as the following expression considering that the power factor is equal to one approximately:

$$\gamma_f = \sqrt{\frac{2+m^2}{2+k^2}}\frac{\sqrt{(m^2+\alpha^2-6m\alpha)^2}}{(m-\alpha)(2-m^2)}. \tag{28}$$

The proportion of the FBSM voltage fundamental frequency fluctuations which can be seen as a function of modulation index and the variable α is similar to the aforementioned analysis in Section III. Its 3-D surface which is presented in Fig. 6 is depicted by MATLAB with the same method.

According to Fig. 6, the function of the proportion has almost no noticeable change when the modulation index varies. However, a dramatic change of the function with the variable α is obvious. Furthermore, the function of the proportion exists a zero point which is the root of the quadratic equation in the denominator of (28). Solving the quadratic equation, the relationship of the variable α and the modulation index is given in (29). The FBSM voltage fundamental frequency fluctuations in F1-MMC would be almost eliminated completely if the variable α and the modulation index satisfy (29) in F2-MMC. Thus, the FBSM capacitance of F2-MMC can be reduced significantly due to that the fluctuations of FBSM voltage mainly contain

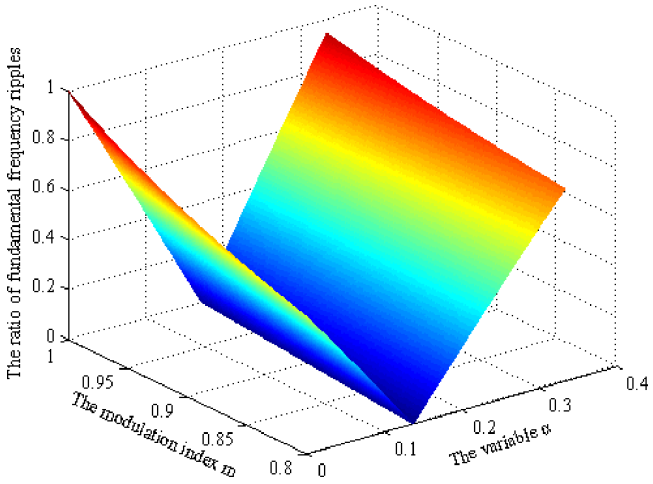

Fig. 6. Proportion of the FBSM voltage fundamental frequency fluctuations of F2-MMC and F1-MMC.

fundamental frequency component:

$$\alpha = \left(3 - 2\sqrt{2}\right) m. \tag{29}$$

Similarly, the second-order harmonic fluctuations of the FBSM voltages of the F2-MMC and F1-MMC can be achieved from (24) and (25). Supposing that the second-order harmonic ripples of the FBSM voltages of the F1-MMC and F2-MMC are ε_{2f1} and ε_{2f2}, respectively. They are presented by the following expression:

$$\varepsilon_{2f2} = \frac{(m+\alpha) I_{o2}}{16\omega C U_c} \tag{30}$$

$$\varepsilon_{2f1} = \frac{m I_{o1}}{16\omega C U_c}. \tag{31}$$

The proportion of the FBSM voltage second-order harmonic fluctuations is obtained by inserting (11) in (30) and (31) under approximate unity power factor conditions. That is

$$\gamma_{2f} = \frac{m+\alpha}{m}\sqrt{\frac{2 + m^2\cos^2\varphi}{2 + k^2\cos^2\varphi}}. \tag{32}$$

The function of the proportion of the FBSM voltage second-order harmonic fluctuations is the same as (14). So its 3-D surface depicted by MATLAB is illustrated in Fig. 5 according to which the FBSM voltage second harmonic fluctuations of F1-MMC and F2-MMC scarcely change. Hence, the second harmonic fluctuations of F2-MMC are considered to be the same as that of F1-MMC due to its small amplitude in FBSM voltage fluctuations. In summary, the FBSM capacitance of F2-MMC will research the minimum in case that (29) is satisfied. As is known in HVdc applications, large amount of module capacitances are bulky and extremely expensive. So, reducing FBSM capacitance significantly has great benefits to HVdc systems. Meanwhile, the variable α nearly has no influence on the power transmission capability of the F2-MMC when it ranges from $0.115m$ to $0.172m$. Hence, the F2-MMC operated with (29) is considered as the optimal design with low energy storage requirements for HVdc transmission systems.

V. Circulating Current Analysis and Arm Inductor Design

A. Circulating Current Analysis

Circulating current especially the second-order harmonic component has a significant impact on FBSM capacitor voltage fundamental frequency and second-order fluctuations despite its small amplitude. Therefore, it is necessary to analyze the circulating currents of F1-MMC and F2-MMC. Assuming that the circulating currents of F1-MMC and F2-MMC are i_{2f1} and i_{2f2} and their amplitude are I_{2f1} and I_{2f2}, respectively. Thus, (18) and (19) are rewritten as follows:

$$i_{au2} = \frac{I_{o2}}{4}\frac{m+\alpha}{m-\alpha}\cos\varphi + \frac{I_{o2}}{2}\cos(\omega t - \varphi) + i_{2f_2} \tag{33}$$

$$i_{au1} = \frac{I_{o1}}{4} m\cos\varphi + \frac{I_{o1}}{2}\cos(\omega t - \varphi) + i_{2f_1}. \tag{34}$$

Neglecting the arm equivalent resistance, the upper and the lower arm voltages should meet Kirchhoff's voltage law with the definition that the arm inductor is L. That is given by

$$NS_{au}u_{cau} + NS_{al}u_{cal} + 2L\frac{di_{2f}}{dt} = U_{\rm dc}. \tag{35}$$

Substituting (20)–(23), (29), (33), and (34) into (35), the circulating currents of the F2-MMC and F1-MMC are derived under unity power factor condition. That is

$$I_{2f_2} = \frac{\left(3\sqrt{2}-4\right) m^2 I_{o2}}{\frac{16\omega^2 LC}{N_2} - \frac{\left(84-56\sqrt{2}\right)m^2}{3}} \tag{36}$$

$$I_{2f_1} = \frac{I_{o1}\left(3m - m^3\right)}{\frac{64\omega^2 LC}{N_1} - 4\left(1 + \frac{2m^2}{3}\right)}. \tag{37}$$

According to (36) and (37), the ratio of the amplitude of circulating currents of F2-MMC and F1-MMC is nonlinear about arm inductor and FBSM capacitance. The FBSM capacitor voltage fundamental frequency fluctuations resulted by circulating currents mainly come from the circulating currents multiplied by the dc components of equivalent switching function. Meanwhile, its second-order harmonic fluctuations mainly come from the circulating currents multiplied by the ac components of equivalent switching function. So, the FBSM capacitor voltage fundamental frequency fluctuations of F2-MMC are smaller than F1-MMC while its second-order harmonic fluctuations are larger if $I_{2f2} = I_{2f1}$ according to (20) and (21). Therefore, the FBSM capacitor voltage fundamental frequency and second-order harmonic fluctuations produced by circulating currents can be considered as the same since the amplitude of circulating current is small. The amplitude of the circulating currents of F1-MMC and F2-MMC can represent the FBSM voltage fluctuations.

B. Arm Inductor Design

The analyses about RMS of arm currents in Section III do not contain the circulating currents. Hence, the following constraint condition should meet by selecting appropriate arm inductor and FBSM capacitance in order to guarantee the same current

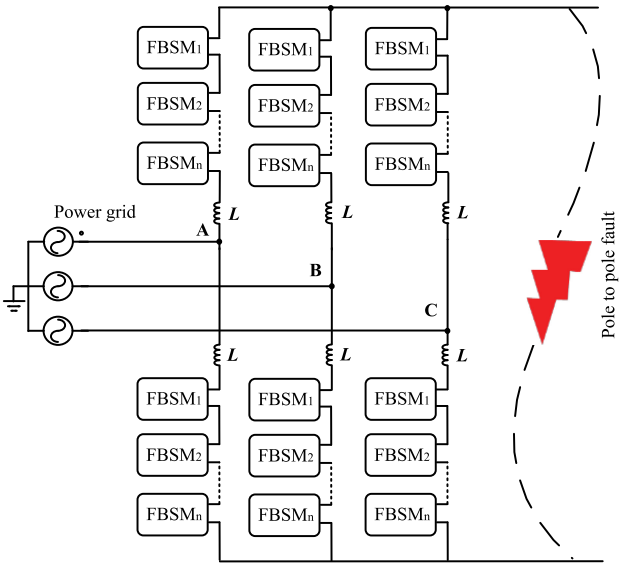

Fig. 7. Schematic diagram of the simulated F-MMC for HVdc systems.

TABLE I
MAIN CIRCUIT PARAMETERS OF F1-MMC AND F2-MMC

MMC configuration	F1-MMC	F2-MMC
Rated apparent power [MVA]	412	544
Rated active power [MW]	400	528
Rated reactive power [MVar]	100	132
DC voltage [kV]	±160	±160
AC voltage (rms) [kV]	176	277
Number of FBSMs per arm	200	268
FBSM capacitance [mF]	12	6.5
Arm inductance [mH]	55	66
FBSM average voltage [kV]	1.6	1.6

stress of F1-MMC and F2-MMC:

$$I_{2f_1} = I_{2f_2}. \tag{38}$$

VI. SIMULATION RESULTS

In order to verify the validity of the analyses in Sections III and IV, the full-scale simulations of F1-MMC and F2-MMC have been implemented. A simplified schematic diagram of the simulated system is shown in Fig. 7. Employing the Thevenin equivalent circuit method for reducing simulation time without affecting accuracy [33], the main circuit parameters of the F1-MMC and the F2-MMC are presented in Table I in which the modulation index and the variable α are 0.9 and 0.155, respectively. So, the number of FBSMs per arm of F2-MMC is 34% more than that of F1-MMC according to (9). Meanwhile, the power transferred by F2-MMC is 32% higher than the F1-MMC which is calculated from (13). The number of FBSMs per arm and rated power of the F2-MMC are 268 and 544 MVA presented in Table I. The FBSM voltage fundamental frequency fluctuations of F2-MMC are almost eliminated under unity power factor condition according to (29). The FBSM voltage second-order harmonic fluctuations introduced in Sections IV and V have almost no change seen from (32) and (38). Moreover, the FBSM voltage fundamental frequency fluctuations are about two times of second-order harmonic fluctuations. This is shown in Fig. 8 which is achieved by fast Fourier transform (FFT) of the upper arm FBSM average voltage of phase A. Considering a small amount of fundamental frequency fluctuations resulted by circulating currents, the FBSM capacitance of the F2-MMC can be smaller than half of the FBSM capacitance of the F1-MMC. However, the reactive power which is not concerned in Sections IV and V can result in fundamental frequency fluctuations. So, the FBSM capacitance of F2-MMC is a little more than half of the FBSM capacitance of the F1-MMC in order to achieve the same fluctuations. Therefore, the FBSM capacitance of the F1-MMC is 12 mF while the F2-MMC FBSM capacitance is 6.5 mF. Additionally, the arm inductor of the F2-MMC can be calculated as 66 mH from (38).

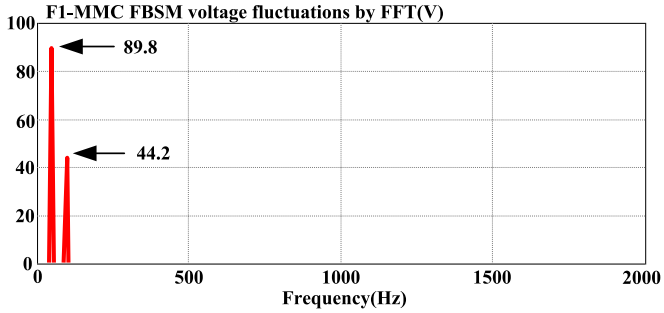

Fig. 8. Amplitude of the fundamental frequency and second-order harmonic of the F1-MMC FBSM voltage fluctuations by FFT.

A. Normal Operation

The simulation results of the F1-MMC during normal operation are shown in Fig. 9. In this simulation, the operating apparent power of the F1-MMC is 412 MVA which is composed of 400 MW and 100 MVar. The dc-bus voltage and dc-side current are depicted in Fig. 9(a) and (b), respectively. The amplitude of ac-side current which is presented in Fig. 9(c) is close to 2 kA. Fig. 9(d) and (e) shows the upper arm and the lower arm currents which range from –1158 to 818 A. The RMS of arm currents are about 821 A. The FBSM average voltages of the upper arm are depicted in Fig. 9(f) while the average voltages of the lower arm are provided in Fig. 9(g). The FBSM average voltages change from about 1475 V to around 1725 V.

Fig. 10 shows the steady-state simulation results of the F2-MMC operated with 528 MW active power and 132 MVar reactive power. The dc-bus voltage is the same as the F1-MMC while the dc-side current is bigger; see Fig. 10(a) and (b). The amplitude of ac-side current described in Fig. 10(c) is about 1600 A owing to the higher ac-side voltage compared to the F1-MMC. As shown in Fig. 10(d) and (e), the upper arm and lower arm currents of the F2-MMC range from –1210 to 605 A. The positive maximum is smaller than that of F1-MMC while the negative maximum is bigger since the smaller FBSM capacitance leads to larger circulating current. The RMS of arm currents are about 825 A which is almost the same as that of the F1-MMC. In Fig. 10(f) and (g), the FBSM average voltages of the upper and

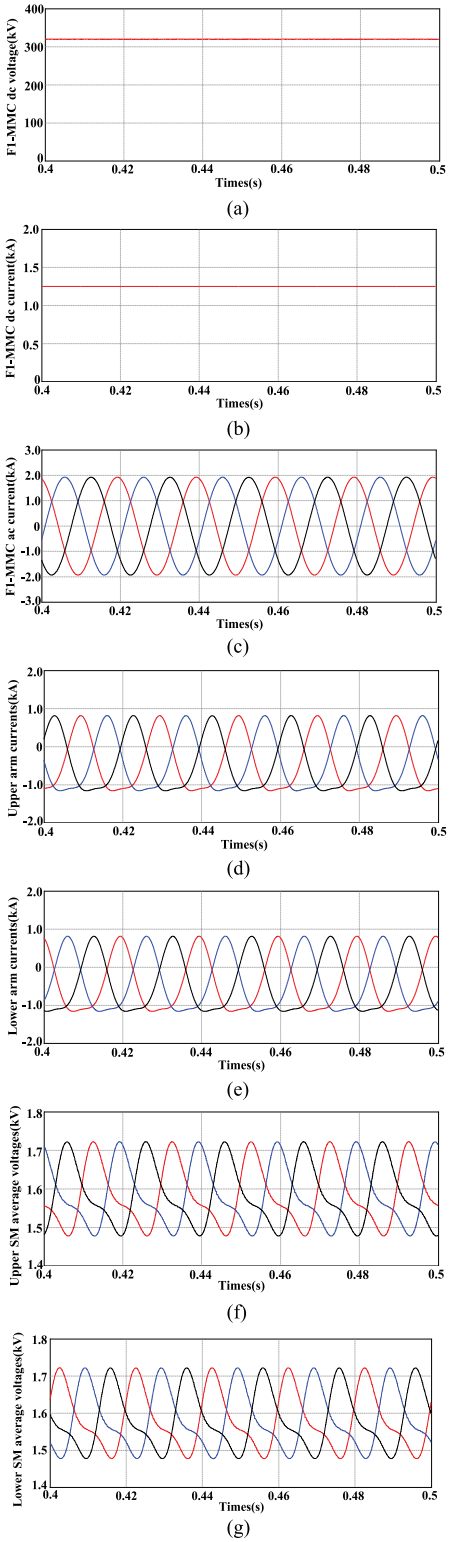

Fig. 9. Simulation results of the F1-MMC in normal operation.

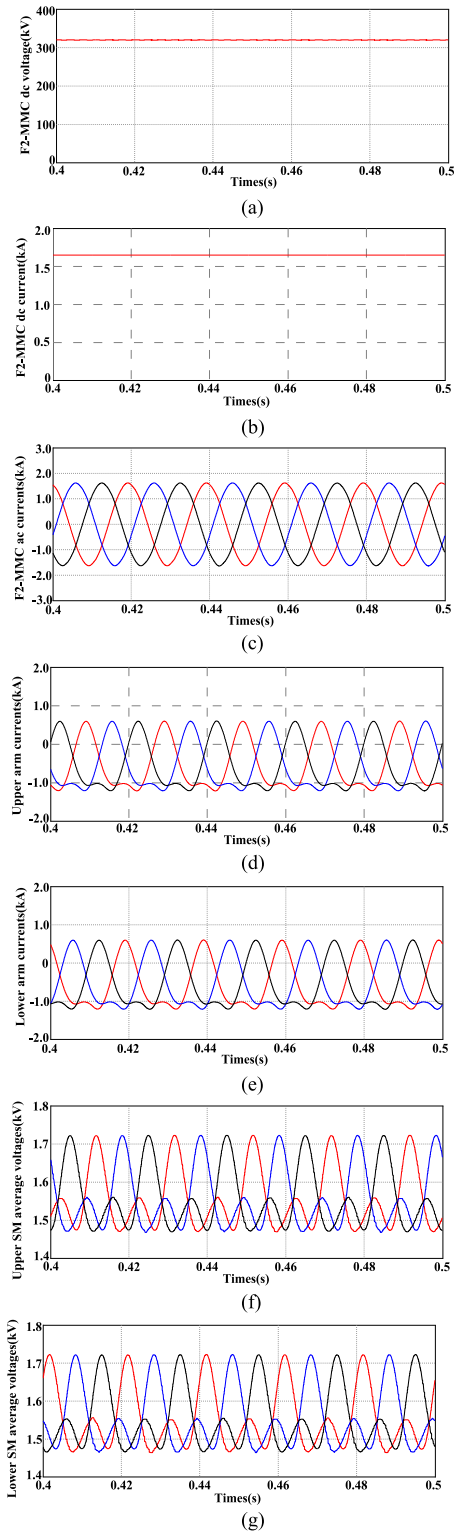

Fig. 10. Simulation results of the F2-MMC in normal operation.

the lower arm are presented, respectively. The average voltages change from around 1471 V to about 1723 V which is very close to that of the F1-MMC. See Fig. 10(f) and (g); the FBSM average voltages mainly include second-order harmonic fluctuations which coincides with the analyses in Section IV compared to Fig. 9(f) and (g). However, the FBSM average voltages still contain fundamental frequency fluctuations which mainly come from two parts. The first one is that the circulating currents ignored in Section IV multiplied by the equivalent switching function can result in fundamental frequency fluctuations. The second one comes from that the reactive power of the F2-MMC

is 132 MVar. The reactive power would lead to fundamental frequency fluctuations in FBSM voltages according to (26).

B. Fault Blocking Capability

Fig. 11 presents the simulation results of the dynamic performance of the F1-MMC when a pole-to-pole dc short-circuit fault occurs. Before $t = 1$ s, the transmission systems of the F1-MMC delivered 400 MW active power. At $t = 1$ s, a dc short-circuit fault happens and the short-circuit impedance was set as $2\,\Omega/0.1$ mH. This is a temporary fault which continued 0.1 s. The dc-side current, dc positive and negative voltage of the F1-MMC are always measured and the dc short-circuit fault is consider to occur when the difference between dc positive and negative voltage is lower than 200 kV and the dc-side current is larger than 500 A at the same time. After a delay time of 280 μs, the F1-MMC turned all IGBTs off and the dc-side current shown in Fig. 11(b) was reduced to zero quickly. The ac-side current and the arm currents of the upper and the lower arm also became zero due to the arm reverse voltages which are depicted in Fig. 11(c), (d), and (e), respectively. The maximum of the dc-side current was about 3800 A while the maximum of the arm currents was around 2500 A during the failure time. In addition, the FBSM voltages presented in Fig. 11(f) and (g) did not change since the arm currents were reduced to zero during the fault period. At $t = 1.1$ s, the fault was cleared and the system restarted to normal operation.

Correspondingly, the dynamic performance of the F2-MMC is illustrated in Fig. 12. Both the F1-MMC and F2-MMC had the same short-circuit impedance and the power transferred by the F2-MMC was 528 MW. Besides, the dc short-circuit fault detection method of the F2-MMC is the same as that of F1-MMC. All IGBTs of the F2-MMC were blocked with the same fault detection principle after the same delay time. The dc short-circuit fault lasted for 0.1 s. The dc-side current, the ac-side current, and the arm currents of the upper and the lower arm are described in Fig. 12(b), (c), (d) and (e), respectively. The dynamic performance of the F2-MMC during fault period is very similar to the F1-MMC. The maximum value the dc-side current and the arm currents researched was 3800 and 2300 A. The FBSM average voltages of the upper and the lower arm are presented in Fig. 12(f) and (g). It is worth mentioning that the FBSM average voltages of the F2-MMC range from about 1500 V to around 1705 V under pure active power conditions. The fluctuations are smaller than that in Fig. 11(f) and (g). The analyses in Section IV are verified that the greater the power factor, the smaller the FBSM voltage fluctuations of the F2-MMC. Then, the F2-MMC restarted to normal operation with the short-circuit fault eliminated at $t = 1.1$ s.

C. Fault Ride Through Capability

In this section, the dc short-circuit fault ride through capability of the F1-MMC and F2-MMC was demonstrated. The simulation results of the dynamic performance of the F1-MMC are presented in Fig. 13 under dc short-circuit fault conditions. In normal operation mode, the power of the F1-MMC flowed from the ac side to the dc side was 400 MW. At $t = 1$ s, the dc

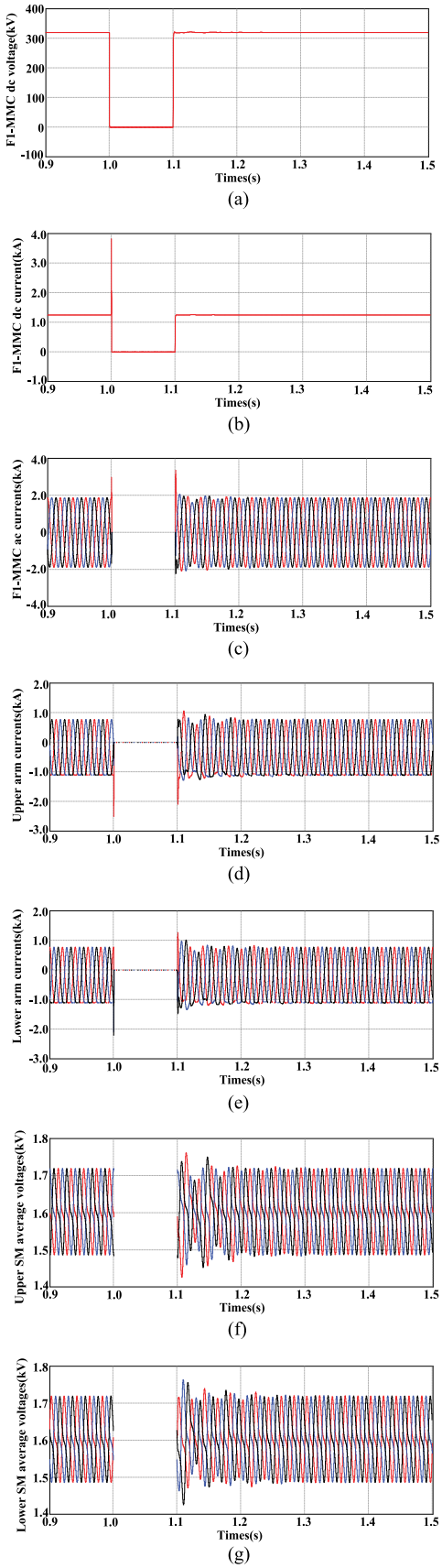

Fig. 11. Simulation results of the F1-MMC with a block strategy under dc short-circuit fault conditions.

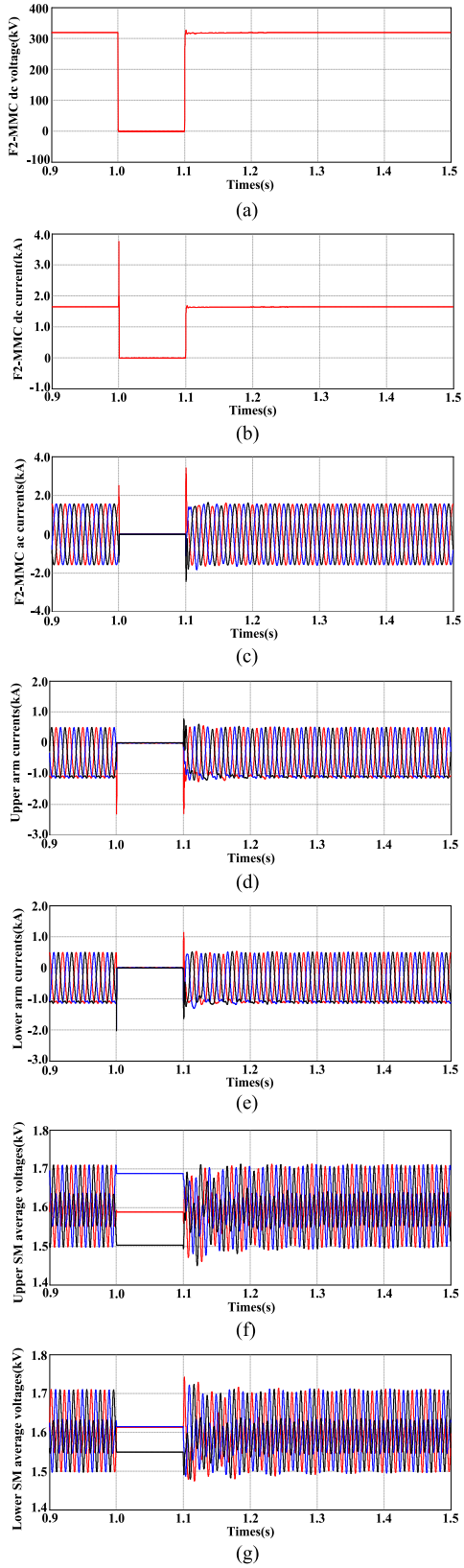

Fig. 12. Simulation results of the F2-MMC with a block strategy under dc short-circuit fault conditions.

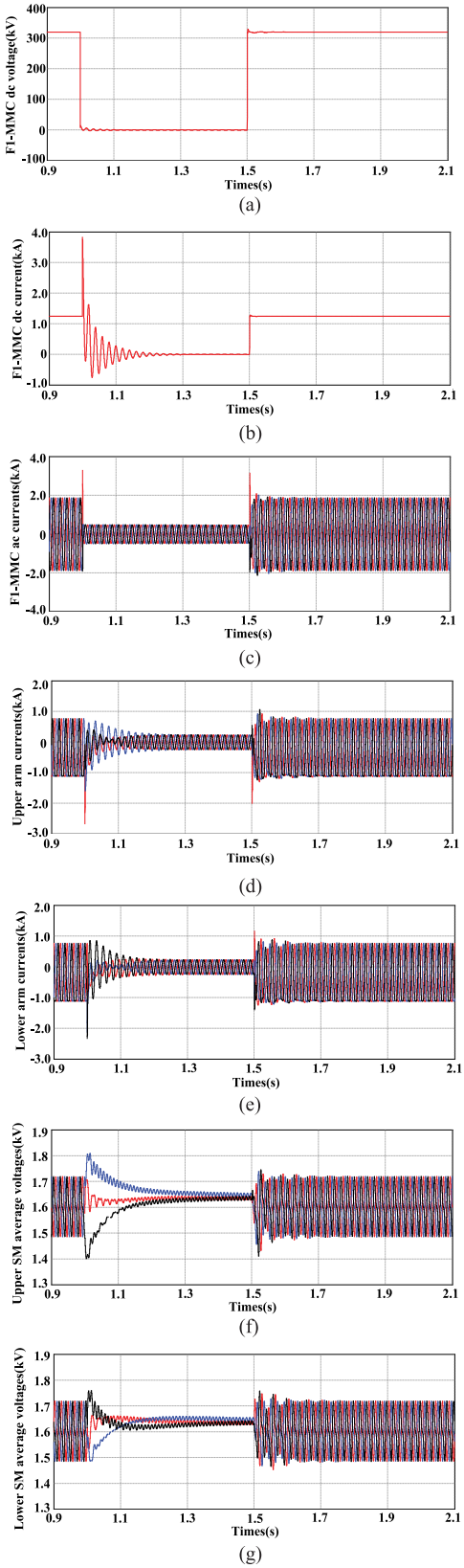

Fig. 13. Simulation results of the F1-MMC with a ride through strategy under dc short-circuit fault conditions.

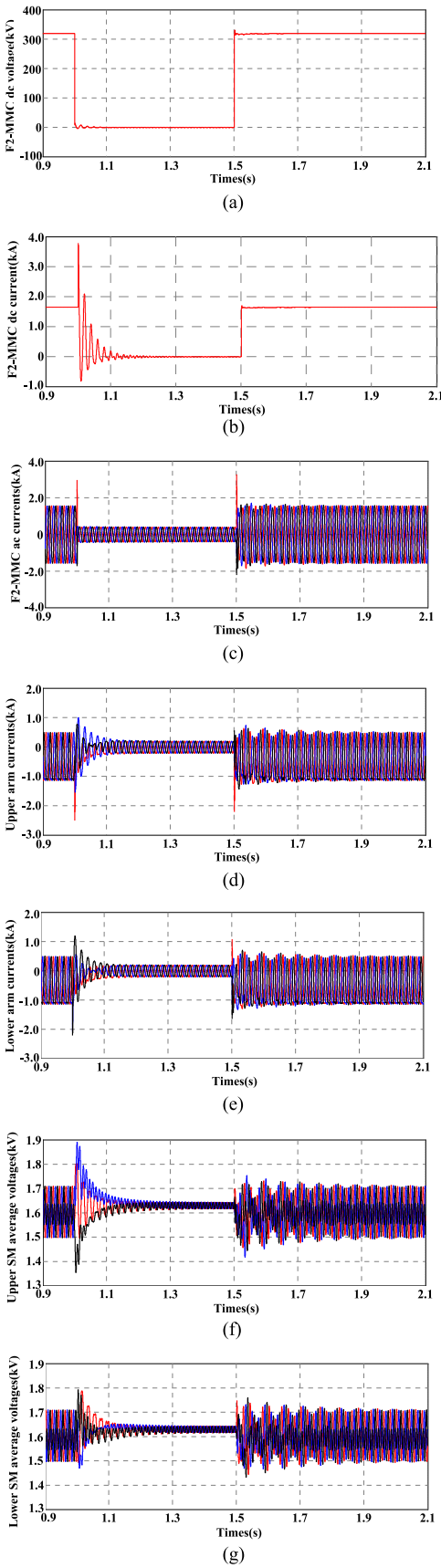

Fig. 14. Simulation results of the F2-MMC with a ride through strategy under dc short-circuit fault conditions.

short-circuit fault which lasted for 0.5 s happened with the short-circuit impedance sat as $4\,\Omega/0.1$ mH. The fault detection method and the delay time of the F1-MMC and F2-MMC were the same as that in Section VI-B. After 0.2 s of oscillation, the dc-side current shown in Fig. 13(b) was reduced to zero. During the fault period, the F1-MMC provided 100 MVar reactive power to support the grid voltage which is presented in Fig. 13(c). In Fig. 13(d) and (e), the arm currents of the upper and the lower arm were provided while they became sine waves during fault. The peak value of the dc-side current and arm currents was about 3850 and 2666 A, respectively. See Fig. 13(f) and (g); the maximum of FBSM voltage reached 1800 V while the minimum reached 1400 V during fault period. Finally, the F1-MMC was recovered at $t = 1.5$ s to normal operation when the fault was cleared.

The simulation results of the dynamic performance of the F2-MMC are presented in Fig. 14 under dc short-circuit fault conditions. The power transferred by the F2-MMC was 528 MW during normal operation. The fault continued 0.5 s and the short-circuit impedance was also sat as $4\,\Omega/0.1$ mH. The dc-side current depicted in Fig. 14(b) became almost zero with oscillation for about 0.15 s. As shown in Fig. 14(c), 132 MVar reactive power was provided by the F2-MMC in order to support grid voltage. The peak value of the dc-side current reached about 3800 A while the maximum of arm currents was around 2500 A which was illustrated in Fig. 14(d) and (e). In Fig. 14(f) and (g), the maximum and minimum of the FBSM voltages were 1880 and 1360 V which were larger than that in Fig. 13(f) and (g). This was mainly caused by small FBSM capacitance of the F2-MMC. After the fault eliminating, the system of the F2-MMC restarted to normal operation at $t = 1.5$ s.

VII. Conclusion

This paper presents the analyses about theF-MMC utilizing the negative voltage state of FBSM. The analyses demonstrate that the power transmission capability of a single FBSM of the F-MMC with using negative voltage state is very close to that of the F-MMC without using the negative voltage state if the modulation index is high. The optimization of parameter for the power transmission capability of a single FBSM is also proposed under the same dc voltage and RMS of arm currents conditions. In the meantime, the fundamental frequency fluctuations of the FBSM voltage are inhibited obviously if the F-MMC is operated under pure active power conditions. The optimization of parameter presented in this paper indicates that the FBSM capacitance can be reduced to nearly half of the original. The design method is also provided. The F-MMC designed in this paper can provide a space-saving and cost-effective converter for HVdc transmission systems. Simulation results verify the proposed parameter design method. Its dc short-circuit fault blocking and ride through capability are also validated.

References

[1] J. Beerten, S. Cole, and R. Belmans, "Modeling of multi-terminal VSC HVDC systems with distributed DC voltage control," *IEEE Trans. Power Syst.*, vol. 29, no. 1, pp. 34–42, Jan. 2014.

[2] N. Flourentzou, V. G. Agelidis, and G. D. Demetriades, "VSC-based HVDC power transmission systems: An overview," *IEEE Trans. Power Electron.*, vol. 24, no. 3, pp. 592–602, Mar. 2009.
[3] A. Lesnicar and R. Marquardt, "An innovative modular multilevel converter topology suitable for a wide power range," in *Proc. IEEE PowerTech Conf.*, Bologna, Italy, Jun. 23–26, 2003.
[4] S. Debnath, J. Qin, B. Bahrani, M. Saeedifard, and P. Barbosa, "Operation, control, and applications of the modular multilevel converter: A review," *IEEE Trans. Power Electron.*, vol. 30, no. 1, pp. 37–53, Jan. 2015.
[5] Q. Jiangchao and M. Saeedifard, "Predictive control of a modular multilevel converter for a back-to-back HVDC system," *IEEE Trans. Power Del.*, vol. 27, no. 3, pp. 1538–1547, Jul. 2012.
[6] M. A. Perez, J. Rodriguez, E. J. Fuentes, and F. Kammerer, "Predictive control of AC–AC modular multilevel converters," *IEEE Trans. Ind. Electron.*, vol. 59, no. 7, pp. 2832–2839, Jul. 2012.
[7] A. Nami, J. Liang, F. Dijkhuizen, and G. D. Demetriades, "Modular multilevel converters for HVDC applications: Review on converter cells and functionalities," *IEEE Trans. Power Electron.*, vol. 30, no. 1, pp. 18–36, Jan. 2015.
[8] J. Peralta, H. Saad, S. Dennetière, J. Mahseredjian, and S. Nguefeu, "Detailed and averaged models for a 401-level MMC-HVDC system," *IEEE Trans. Power Del.*, vol. 27, no. 3, pp. 1501–1508, Jul. 2012.
[9] R. Li, G. P. Adam, D. Holliday, J. E. Fletcher, and B. W. Williams, "Hybrid cascaded modular multilevel converter with DC fault ride-through capability for the HVDC transmission system," *IEEE Trans. Power Del.*, vol. 30, no. 4, pp. 1853–1862, Aug. 2015.
[10] G. Tang, Z. Xu, and Y. Zhou, "Impacts of three MMC-HVDC configurations on AC system stability under DC line faults," *IEEE Trans. Power Syst.*, vol. 29, no. 6, pp. 3030–3040, Nov. 2014.
[11] J. M. Meyer and A. Rufer, "A DC hybrid circuit breaker with ultra-fast contact opening and integrated gate-commutated thyristors (IGCTs)," *IEEE Trans. Power Del.*, vol. 21, no. 2, pp. 646–651, Apr. 2006.
[12] C. Meyer, M. Kowal, and R. W. De Doncker, "Circuit breaker concepts for future high-power DC-applications," in *Proc. 40th Ind. Appl. Soc. Annu. Meeting Conf.*, Oct. 2–6, 2005, pp. 860–866.
[13] J. Candelaria and J.-D. Park, "VSC-HVDC system protection: A review of current methods," in *Proc. IEEE Power Energy Soc. Power Syst. Conf. Expo.*, Mar. 20–23, 2011, pp. 1–7.
[14] C. Meyer and R. W. De Doncker, "LCC analysis of different resonant circuits and solid-state circuit breakers for medium-voltage grids," *IEEE Trans. Power Del.*, vol. 21, no. 3, pp. 1414–1420, Jul. 2006.
[15] X. Li, Q. Song, W. Liu, H. Rao, and L. Li, "Protection of nonpermanent faults on DC overhead lines in MMC based HVDC systems," *IEEE Trans. Power Del.*, vol. 28, no. 1, pp. 483–490, Jan. 2013.
[16] C. Chao, G. P. Adam, S. J. Finney, and B. W. Williams, "DC power network post-fault recharging with an H-bridge cascaded multilevel converter," in *Proc. 28th Annu. IEEE Appl. Power Electron. Conf. Expo.*, Mar. 17–21, 2013, pp. 2569–2574.
[17] G. P. Adam and I. E. Davidson, "Robust and generic control of full-bridge modular multilevel converter high-voltage DC transmission systems," *IEEE Trans. Power Del.*, vol. 30, no. 6, pp. 2468–2476, Dec. 2015.
[18] R. Marquardt, "Modular multilevel converter topologies with DC-short circuit current limitation," in *Proc. Int. Power Electron. Conf. ECCE-Asia*, May 30–Jun. 3, 2011, pp. 1425–1431.
[19] J. Qin, M. Saeedifard, A. Rockhill, and R. Zhou, "Hybrid design of modular multilevel converters for HVDC systems based on various submodule circuits," *IEEE Trans. Power Del.*, vol. 30, no. 1, pp. 385–394, Feb. 2015.
[20] J. Xu, C. Zhao, Z. He, and Y. Guo, "Start-up control and DC fault ride-through strategies of a hybrid MMC-HVDC system suitable for overhead line transmission," in *Proc. IEEE 2nd Int. Further Energy Electron. Conf.*, Nov. 1–4, 2015, pp. 1–6.
[21] S. Cui and S. Sul, "A comprehensive DC short circuit fault ride through strategy of hybrid modular multilevel converters (MMCs) for overhead line transmission," *IEEE Trans. Power Electron.*, vol. 31, no. 11, pp. 7780–7796, Nov. 2016.
[22] S. Cui, S. Kim, J. Jung, and S. Sul, "Principle, control and comparison of modular multilevel converters (MMCs) with DC short circuit fault ride-through capability," in *Proc. 29th Annu. IEEE Appl. Power Electron. Conf. Expo.*, Mar. 16–20, 2014, pp. 610–616.
[23] R. Zeng, L. Xu, L. Yao, and B. W. Williams, "Design and operation of a hybrid modular multilevel converter," *IEEE Trans. Power Electron.*, vol. 30, no. 3, pp. 1137–1146, Mar. 2015.
[24] A. Lesnicar, "Neuartiger, modularer mehrpunktumrichter M2C fur netzkupplungsanwendungen," Ph.D. dissertation, Dept. Elect. Eng. Inf. Technol., Univ. Bundeswehr, Munich, Germany, 2008.
[25] Q. Song, W. Liu, X. Li, H. Rao, S. Xu, and L. Li, "A steady state analysis method for a modular multilevel converter," *IEEE Trans. Power Electron.*, vol. 28, no. 8, pp. 3702–3713, Aug. 2013.
[26] K. Ilves, S. Norrga, L. Harnefors, and H. P. Nee, "On energy storage requirements in modular multilevel converters," *IEEE Trans. Power Electron.*, vol. 29, no. 1, pp. 77–88, Jan. 2014.
[27] H. Barnklau, A. Gensior, and S. Bernet, "Submodule capacitor dimensioning for modular multilevel converters," in *Proc. IEEE Energy Convers. Congr. Expo.*, Sep. 15–20, 2012, pp. 15–20.
[28] S. P. Engel and R. W. De Doncker, "Control of the modular multi-level converter for minimized cell capacitance," in *Proc. 14th Eur. Power Electron. Appl.*, Aug. 30–Sep. 1, 2011, pp. 1–10.
[29] J. Pou, S. Ceballos, G. Konstantinou, V. G. Agelidis, R. Picas, and J. Zaragoza, "Circulating current injection methods based on instantaneous information for the modular multilevel converter," *IEEE Trans. Ind. Electron.*, vol. 62, no. 2, pp. 777–788, Feb. 2015.
[30] R. Picas, S. Ceballos, J. Pou, J. Zaragoza, G. Konstantinou, and V. G. Agelidis, "Closed-loop discontinuous modulation technique for capacitor voltage ripples and switching losses reduction in modular multilevel converters," *IEEE Trans. Power Electron.*, vol. 30, no. 9, pp. 4714–4725, Sep. 2015.
[31] K. Ilves, A. Antonopoulos, L. Harnefors, S. Norrga, L. Angquist, and H. P. Nee, "Capacitor voltage ripple shaping in modular multilevel converters allowing for operating region extension," in *Proc. 37th IEEE Annu. Conf. Ind. Electron. Soc.*, Nov. 7–10, 2011, pp. 4403–4408.
[32] Z. Li *et al.*, "Power module capacitor voltage balancing method for a ±350 kV/1000 MW modular multilevel converter," *IEEE Trans. Power Electron.*, vol. 31, no. 6, pp. 3977–3984, Jun. 2016.
[33] U. Gnanarathna, A. Gole, and R. Jayasinghe, "Efficient modeling of modular multilevel HVDC converters (MMC) on electromagnetic transient simulation programs," *IEEE Trans. Power Del.*, vol. 26, no. 1, pp. 316–324, Jan. 2011.

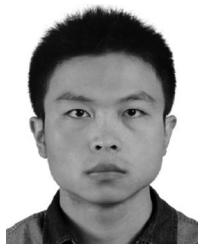

Cong Zhao (S'16) was born in Liaoning Province, China, in 1988. He received the B.S. degree in electrical engineering from Tsinghua University, Beijing, China, in 2012. Since September 2012, he has been working toward the Ph.D. degree in power electronics and power drives in the Institute of Electrical Engineering, Chinese Academy of Sciences, Beijing.

His research interests include circuit topology, analysis and control of modular multilevel converter, especially its applications in high voltage direct current fields.

Yaohua Li was born in Henan, China, in 1966. He received the Ph.D. degree in power electronics and power drives from Tsinghua University Beijing, China, in 1994.

From 1995 to 1997, he was a Postdoctoral Research Fellow in the Institute of Electrical Machine, Technical University of Berlin, Germany. He joined the Institute of Electrical Engineering, Chinese Academy of Sciences, Beijing, in 1997, where he is currently a Professor and Vice Director of this institute. His research fields include analysis and control of electrical machines, power electronics, etc.

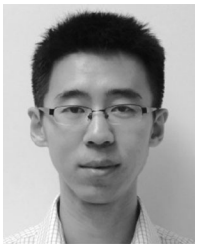

Zixin Li (S'08–M'10–SM'16) was born in Hebei Province, China, in 1981. He received the B.Eng. degree in industry automation from North China University of Technology, Beijing, China, in 2001, and the Ph.D. degree with honor in power electronics and power drives from the Institute of Electrical Engineering, Chinese Academy of Sciences, Beijing, in 2010.

He joined the Institute of Electrical Engineering, Chinese Academy of Sciences, in 2010, where he is currently a Professor. Dr. Li is also an Associate Editor of IEEE Transactions on Power Electronics. His research interests include circuit topology, control and analysis of power converters, especially multilevel converters in high-power fields.

Dr. Zixin Li has authored and coauthored more than 60 academic papers and holds 5 invention patents in China. He also received many honors and awards from IEEE and the government. He was the winner of IEEE Power Electronics Society Richard M. Bass Outstanding Young Power Electronics Engineer Award of 2015 for his contributions to multilevel and HVdc converters.

Ping Wang was born in Shanghai, China, in 1955. He received the B.S. degree in computer science from Lanzhou University, Lanzhou, China, in 1980.

Since 1980, he has been with the Institute of Electrical Engineering, Chinese Academy of Sciences, Beijing, China, where he become an Assistant Engineer in 1985, a Senior Engineer in 1993, and a Professor of power electronics and power drives in 2008. From 1995 to 1996, he was a Visiting Researcher with Fraunhofer Institute for Production Systems and Design Technology Berlin, Germany. His research fields include power electronics, static power converters, active filter, ac drives etc.

Mr. Wang is a member of China Electrotechnical Society.

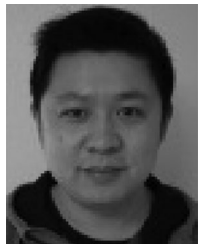

Xun Ma was born in Shandong Province, China, in 1983. He received the B.S. degree in electrical engineering from Dalian University of Technology, Dalian, China, in 2006, and the Ph.D. degree in power electronics and power drives from the Institute of Electrical Engineering, Chinese Academy of Sciences (IEECAS), Beijing, China, in 2012.

He is currently an Associate Professor in IEECAS. His research interests include electric traction ac drive systems, analysis and control of modular multilevel converter applied in high voltage direct current fields.

Yongjie Luo was born in Chongqing, China. He received the B.Eng. degree in electrical engineering from Tsinghua University, Beijing, China, in 2010, and the Ph.D. degree in power electronics and power drives from the Institute of Electrical Engineering, Chinese Academy of Sciences, Beijing, in 2016.

He is currently a Research Engineer in the State Grid Sichuan Electric Power Research Institute, Chengdu, China. His research interests include the modular multilevel converter, multiterminal HVdc, control and protection of power system with high-power electronic devices.